



Regular article

Indentation size effect for spherical nanoindentation on nanoporous gold

Young-Cheon Kim^{a,1,2}, Eun-Ji Gwak^{a,1}, Seung-min Ahn^a, Na-Ri Kang^a, Heung Nam Han^b,
Jae-il Jang^c, Ju-Young Kim^{a,d,*}

^a School of Materials Science and Engineering, UNIST (Ulsan National Institute of Science and Technology), Ulsan 44919, Republic of Korea

^b Department of Materials Science and Engineering, Seoul National University, Seoul 08826, Republic of Korea

^c Division of Materials Science and Engineering, Hanyang University, Seoul 04763, Republic of Korea

^d KIST-UNIST Ulsan Center for Convergent Materials, UNIST, Ulsan 44919, Republic of Korea



ARTICLE INFO

Article history:

Received 25 July 2017

Received in revised form 3 September 2017

Accepted 3 September 2017

Available online xxxx

Keywords:

Nanoporous gold

Nanoindentation

Porous materials

Hardness

Indentation size effect

ABSTRACT

We find that the indentation size effect (ISE) occurs during spherical indentation on nanoporous gold (np-Au). The hardness increases as the indenter radius decreases at a fixed representative strain. We prepare np-Au samples with a ligament size of 26 nm by free-corrosion dealloying and perform multiple spherical nanoindentations with nominal indenter radii of 4, 12, and 50 μm . A nanomechanics model for the ISE during spherical indentation is developed, and the model accurately describes the hardness depending on the indenter radius. We also correlate the ISE trends of spherical and Berkovich indentations along with their differences in terms of the representative strain and the indentation work.

© 2017 Acta Materialia Inc. Published by Elsevier Ltd. All rights reserved.

Spherical indentation has been widely studied because unlike geometrically self-similar sharp indenters, spherical indenters introduce various stress–strain fields depending on the indentation depth. Kim et al. [1] proposed a representative stress–strain method using spherical indentation to determine the tensile properties of metals with Hollomon-type strain-hardening behavior. They used the actual contact depth while considering plastic pile-up, derived a representative stress using Tabor's approach [2] by introducing a plastic constraint factor, and optimized the representative strain using a tangent function of the contact angle between the spherical indenter and the sample surface. Pathak and Kalidindi [3] correlated the indentation stress to the indentation strain and the mean pressure on the projected area to the ratio of the contact radius to the indenter radius (a/R). They investigated the effects of experimental conditions such as continuous stiffness measurement (CSM), pop-in events, indenter size, and polishing on the evaluated indentation stress and strain. They also introduced orientation imaging microscopy and Raman spectroscopy combined with spherical indentations to analyze changes in the microstructure of indents. Swadener et al. [4] found that the indentation size effect (ISE) for spherical indentation depended on the indenter radius and not on

the indentation depth as in the case of sharp indentation. This indicates that the ISE for the spherical indenter radius must be considered when spherical nanoindentation is carried out at small scales. To explain the ISE for spherical indentation, geometrically necessary dislocations (GNDs) were assumed to form to accommodate the spherical indent. They developed the following spherical ISE model based on the Nix–Gao model [5]:

$$\frac{H}{H_0} = \sqrt{1 + \frac{R^*}{R_p}}, \quad (1)$$

where H and H_0 are the hardness and the macroscopic hardness, respectively; R^* is the characteristic constant for the spherical ISE; and R_p is the indent radius after spherical indentation. This equation could successfully describe the trends in spherical indentation hardness for annealed iridium and oxygen-free copper samples. Spary et al. [6] performed finite element simulations on materials with different yield strengths to show that the ISE for spherical indentation is related to dislocation generation rather than to dislocation interaction.

Nanoporous gold (np-Au) has recently attracted interest because of its outstanding chemical and physical characteristics, easy fabrication and applications [7–16]. Most investigations on the mechanical behavior of np-Au have been conducted using nanoindentation [17–23] for convenience in sample preparation and experiment execution, considering that np-Au is brittle unlike solid gold. One such finding established by employing nanoindentation is that the strength or hardness of np-Au

* Corresponding author at: School of Materials Science and Engineering, UNIST (Ulsan National Institute of Science and Technology), Ulsan 44919, Republic of Korea.

E-mail address: juyoung@unist.ac.kr (J.-Y. Kim).

¹ These authors contributed to this work equally.

² Present address: System Convergence Technology Division, Mechanical Safety Technology Center, Korea Testing Laboratory, Jinju-si 52852, Republic of Korea.

is strongly dependent on the relative density and the ligament size; this finding is in line with the “smaller is stronger” phenomenon observed in gold nanopillars [24,25]. For np-Au, the hardness has been reported to increase as the indentation depth decreases when using a Berkovich indenter [20,26]. Recently, the present authors suggested an ISE model for np-Au when using a sharp indenter [27]. The ISE model for np-Au is an inverse function of the indentation depth; the function is derived by assuming that the indentation work is consumed in the plastic collapse of np-Au caused by compressive and shear forces. Spherical nanoindentations have been carried out to investigate mechanical behavior of np-Au [26]. As mentioned above, spherical indentations provide hardness for various representative strains. However, it has not been studied the ISE behavior in spherical indentation depending on indenter radius, R . It is important to understand ISE behavior in spherical indentation when measuring macroscopic hardness of np-Au by using spherical indenter.

Here, we investigate the ISE for spherical indentation on np-Au. To exclude the effect of the ligament size and relative density of np-Au on spherical nanoindentation, np-Au samples with a single ligament size of 26 nm are fabricated using the free-corrosion dealloying process. Nanoindentations are performed on the np-Au samples using three spherical indenters with nominal radii of 4, 12, and 50 μm . The ISE for spherical nanoindentation on np-Au is found to depend on the indenter radius, implying that the hardness for spherical nanoindentation decreases as the indenter radius increases at the same representative strain. A nanomechanics model for spherical indentation on np-Au is developed by assuming that the total indentation work is consumed by the plastic collapse in two loading modes represented by normal and shear forces. We investigate the correlation of the ISEs for spherical and sharp (Berkovich) indentations in terms of strain hardening and indentation work.

Np-Au samples with a ligament size of 26 nm were prepared based on the authors' previous work [27]. $\text{Au}_{30}\text{Ag}_{70}$ precursor alloys were fabricated using pure Au and Ag pellets by melting. After homogenization at 800 $^{\circ}\text{C}$ for 72 h under N_2 environment, the precursor alloys were pressed into discs with a thickness of approximately 1 mm using a

universal testing machine (Instron 5982), and both sides of the discs were gently polished using a diamond suspension with a particle size of 0.25 μm . To release possible internal stress in precursor alloys induced by mechanical pressing and polishing, the precursor alloy discs were annealed in a tube furnace in a N_2 environment at 800 $^{\circ}\text{C}$ for 24 h. Nanoporosity was generated by free-corrosion dealloying in a 70% HNO_3 solution for 72 h at room temperature. Ligament sizes were measured by averaging the neck diameters at the centers of ligament connects, which are possibly the thinnest parts in the scanning electron microscope images.

Spherical nanoindentations were created using diamond sphericoconical indenters with nominal tip radii of 4, 12, and 50 μm . We measured the effective radius, R , and the effective indentation depth of each spherical indenter by observing the side views using an optical microscope; the radii were $3.68 (\pm 0.07) \mu\text{m}$ for the 4 μm nominal radius, $11.42 (\pm 0.11) \mu\text{m}$ for the 12 μm nominal radius, and $54.99 (\pm 0.39) \mu\text{m}$ for the 50 μm nominal radius. These effective radius values were used as the indenter radius, R . The effective indentation depth was the maximum height from the tip depth at which the indenter geometry was described by one value of the effective radius (Fig. 1(a)). The maximum indentation depths were less than this effective indentation depth. Spherical nanoindentations were created using the XP module of a G200 nanoindenter (Keysight) with a maximum load capacity of 500 mN in the CSM mode at an indentation strain rate of 0.05 s^{-1} .

The typical spherical indentation force–depth curves for np-Au are presented in Fig. 1. Fig. 2 shows the hardness as a function of the contact radius, a , when $a/R = 0.142$, where R is the indenter radius. $a/R = 0.142$ corresponds to the compressive yield strain, which is discussed in detail below. The hardness and the contact radius were calculated by the Oliver–Pharr method [28]. Fig. 2 shows that the hardness increases as the contact radius decreases; this behavior is similar to the ISE for spherical indentation of solid materials [4]. The hardness values in Fig. 2 were averaged from at least 15 reproducible indentation force–depth curves.

To analyze the ISE for spherical nanoindentation on np-Au, we developed a nanomechanics model based on the authors' previous work [27]. As shown in Fig. 3(a), from the indenter view, the spherical

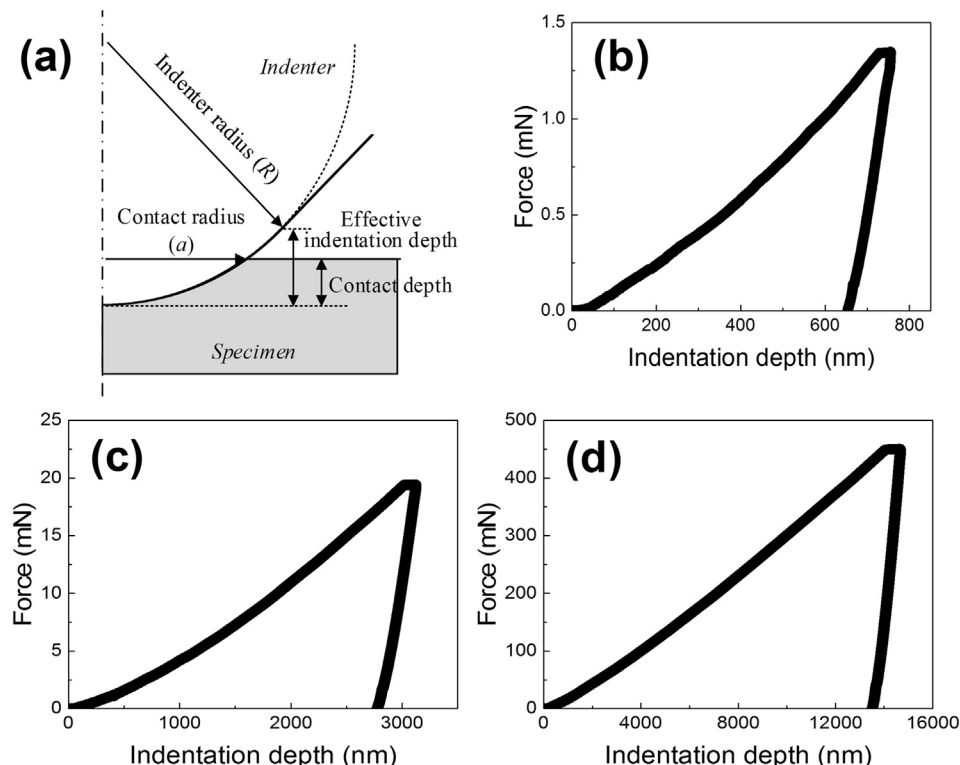


Fig. 1. (a) Schematic diagram of contact morphology, and typical nanoindentation force–depth curves for nominal indenter tip radii of (b) 4, (c) 12, and (d) 50 μm .

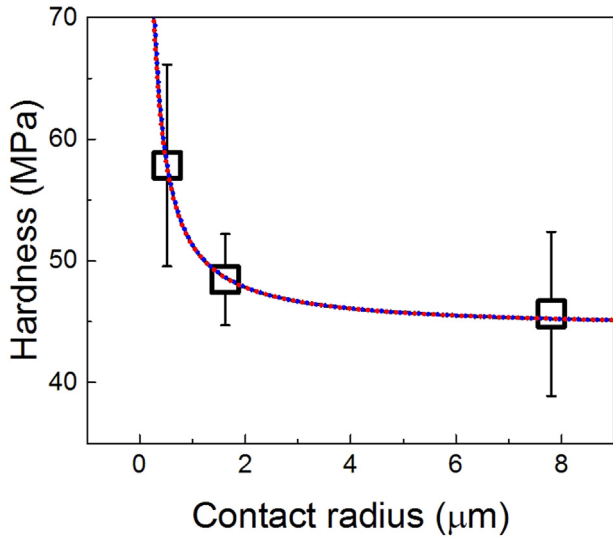


Fig. 2. Relationship between hardness and contact radius for spherical nanoindentation on np-Au. (For interpretation of the references to color in this figure legend, the reader is referred to the web version of this article.)

indenter is regarded as a set of infinitesimal thin flat punches, and from the np-Au view, the total indentation work is considered to be depleted in the plastic collapse of the unit cells of np-Au caused by normal and shear forces. The unit cell D is defined as the length scale and is the sum of one ligament l and one pore (here, the pore size is simply assumed to be $2l$, i.e., $D = 3l$). The indentation force is equal to the

differential of the total indentation work:

$$P = \frac{dW}{dh} = \frac{W_{\text{total}}}{D} = \frac{W_{\text{comp}} + W_{\text{shear}}}{D}. \quad (2)$$

Here, the work dissipated by compressive and shear forces is

$$W_{\text{comp}} = \sigma \cdot \pi r^2 \cdot D, \quad (3)$$

$$W_{\text{shear}} = \tau \cdot 2\pi r \cdot D \cdot k_R D, \quad (4)$$

where σ and τ are the compressive and shear strengths of np-Au, respectively, and k_R is a proportional constant indicating the number of cells deformed along the loading direction by the shear force at the perimeter $2\pi r \cdot D$ when the indentation depth increases by D . As shown in Fig. 3(a), the contact radius a can be described as $R \sin \theta$, where θ is the contact angle between the specimen plane surface and the indenter surface. Combining Eqs. (2)–(4) with Tabor's relation $\sigma = H_0/\Psi$ yields

$$\frac{H}{H_0} = \frac{1}{\Psi} \left(1 + \frac{K_R}{R/D} \right), \quad (5)$$

where H_0 and Ψ are the macroscopic hardness and the plastic constraint factor, respectively, and

$$K_R = \frac{\tau}{\sigma} \cdot \frac{2k_R}{\sin \theta}. \quad (6)$$

Unlike the ISE model for a sharp indenter [27], in which hardness is a function of the normalized indentation depth, Eq. (5) shows that in the spherical indentation on np-Au, the hardness depends on the indenter radius normalized by the unit cell size of np-Au, R/D .

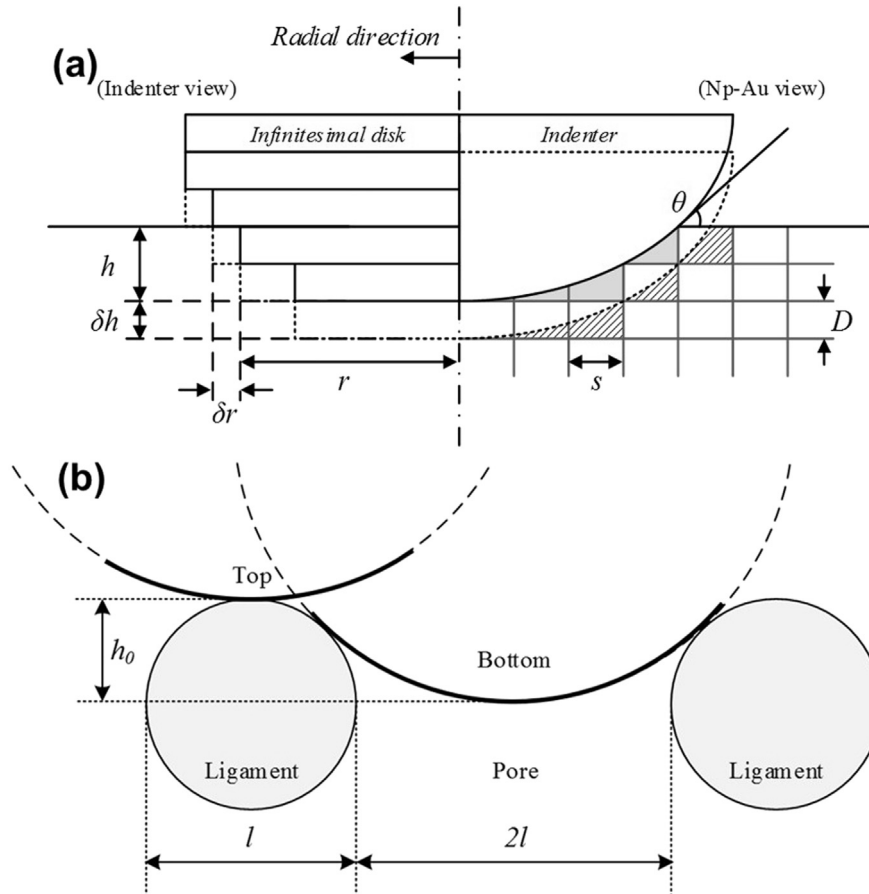


Fig. 3. Schematics for (a) nanomechanics model for spherical nanoindentation on np-Au and (b) initial contact of indenter on ligaments of np-Au.

This equation, when fitted to the experimental values (the solid black line in Fig. 2(a)), properly describes contact-radius-dependent hardness. The characteristic constant K_R and the macroscopic hardness H_0 in Eq. (5) are found to be 2026 and 117.6, respectively, when a plastic constraint factor Ψ of 2.65 is used [29,30]. A k_R value of 339 was evaluated in Eq. (6) by using $\tau/\sigma = 0.42$ and $\sin \theta = 0.142$ (which equals a/R). For the same np-Au sample, k of 2.56 was evaluated for the Berkovich indenter [27]. k_R for the spherical indenter and k for the Berkovich indenter have the same physical meaning: the number of cells deformed along the loading direction by the shear force at the perimeter $2\pi r \cdot D$ when the indentation depth increases by D . Here, the contact angle for spherical indentation, 8.16° , is considerably less than that for Berkovich indentation, 19.7° (from the effective cone angle of 70.3°), which means that during spherical indentation, more cells are deformed along the in-plane direction by penetration as much as D than Berkovich indentation.

Nanoindentation results are analyzed by the Oliver–Pharr method assuming that the initial contact occurs at the flat surface of solid materials. However, in the schematic for the initial contact shown in Fig. 3(b), ligaments and pores are irregularly distributed on the surface, producing surface roughness. The depth difference, h_0 , between the two cases, i.e., contact at the top of the ligament and in the middle of two ligaments, can be described as

$$h_0 = R + \frac{l}{2} - \sqrt{(R + 2l)(R - l)}. \quad (7)$$

Because the hardness values in Fig. 2(a) are averaged from at least 15 reproducible indentation force–depth curves, the average contact depth is simply taken as half of h_0 . The possible deviation in hardness that can be attributed to the surface roughness is approximately 0.4%, 0.04%, and 0.002% for the indenters with nominal radii of 4, 12, and 50 μm , respectively. The deviation in Eq. (7) is shown in Fig. 2(a) as red and blue dotted lines. These lines are almost coincident with the solid black line, which represents the average indenter-size-dependent hardness predicted by Eq. (5). This implies that unlike in the case of Berkovich indentation [27], the effect of the np-Au surface roughness on the results of spherical nanoindentation is negligible.

In contrast to a Berkovich indenter with geometrical self-similarity, the representative strain increases as the indentation depth increases for the spherical indenter. In compression testing, np-Au shows strain hardening during the plastic collapse stage (Fig. 4(a)), which can affect the ISE for spherical indentation. Swadener et al. [4] also found this coupling in the ISE for spherical indentation on solid materials. They compared the hardness values measured by different spherical indenters at the same representative strain, i.e., the same a/R value. In the present study, uniaxial compressive tests were performed on np-Au samples and 0.142 was determined as the a/R value (2.84% representative strain)

to compare the hardness of indenters with nominal radii of 4, 12, and 50 μm . As shown by the compressive stress–strain curve in Fig. 4(a), 2.84% representative strain corresponds to the compressive yield strain, which represents the onset of global plasticity and is expected to minimize the strain-hardening effect in spherical indentation hardness.

Swadener et al. [4] correlated the ISEs for Berkovich and spherical indentations based on the concept of the total length of GNDs in solid materials because GND density is the primary mechanism for the ISE. Following their work, we correlated the ISEs for Berkovich and spherical indentations of np-Au by taking into consideration the indentation work caused by shear force, w_{shear} . According to the mathematics in Eq. (5), the ISE for spherical indentation on np-Au can be attributed to the fact that K_R , which originates from the indentation work caused by shear force, is not zero. The indentation work caused by shear force is the primary mechanism for the ISE during spherical indentation of np-Au. We calculated the indentation work caused by shear force as $w_{\text{shear}} = \tau \cdot 2\pi h (\tan \theta)^{-1} \cdot D \cdot kD$ for a Berkovich indenter and $w_{\text{shear}} = \tau \cdot 2\pi R \sin \theta \cdot D \cdot k_R D$ for a spherical indenter. Considering these two work expressions to be the same yields $R = 0.149h$. Another aspect to be considered in correlating the ISEs for Berkovich and spherical indentations on np-Au is the strain-hardening behavior in the compression of np-Au (Fig. 4(a)). The typical compressive stress–strain curve of porous materials has three stages: linear elasticity, plateau during plastic collapse of ligaments, and sharp increase in stress by densification [31]. While strain hardening is negligible in the plateau stage for porous materials with very low relative densities and uniform ligament sizes, our np-Au sample shows linear strain hardening due to the irregularity of np-Au in terms of the ligament size, shape, distribution with respect to the loading direction, and so on. The difference between the flow stresses corresponding to a representative strain of 7% for a Berkovich indenter and 2.84% for a spherical indenter is 38.5 MPa as shown in Fig. 4(a). This difference is presented on the right and left axes of Fig. 4(b), and $R = 0.149h$, which is derived above, is presented on the top and bottom axes of Fig. 4(b). Fig. 4(b) shows that the ISEs for the Berkovich and spherical indentations on np-Au show similar trends. Based on this correlation, the trend in the ISE for spherical indentations on np-Au is evaluated by that for Berkovich indentations, and vice versa.

We investigated the ISE for spherical indentation on np-Au samples using three different indenters. The indentation depth was set depending on the indenter radius so that the same representative strain was used for consistency in geometrical similarity. We developed a nanomechanics model for the ISE during spherical indentation on np-Au based on two forms of work expended in the plastic collapse caused by the pressing and shearing of internal cells. According to the experimental and modeling results, k_R is considerably greater than k for

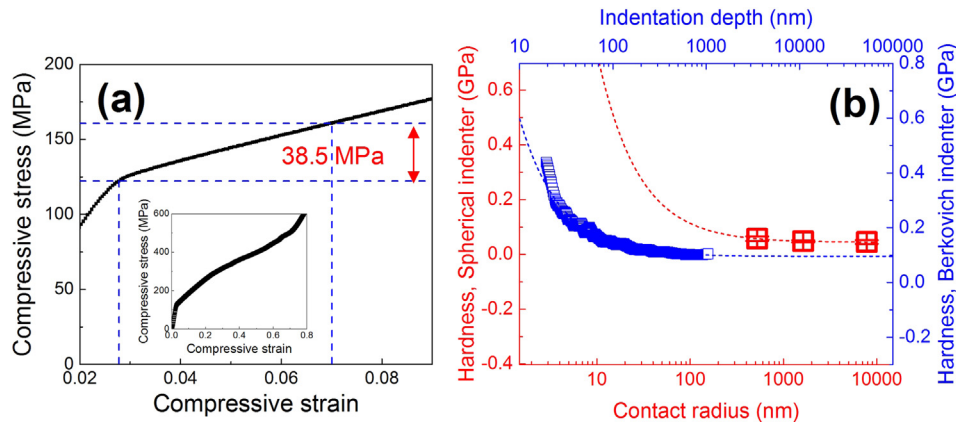


Fig. 4. (a) Typical compressive stress–strain curve of np-Au sample with ligament size of 26 nm that is enlarged one from entire curve presented as inset and (b) hardness correlation between spherical and Berkovich indentations in terms of contact radius and indentation depth.

Berkovich indentation; this might be because more in-plane cells are deformed by the shear force along the loading direction during penetration because of the lower contact angle of the spherical indenter. We correlated the ISEs for the spherical and Berkovich indentations by comparing the strain-hardening behavior in the compressive stress–strain curve in terms of the representative strain and indentation work caused by shear force for each indenter.

Acknowledgments

This work was supported by the National Research Foundation of Korea (NRF) grant funded by the Ministry of Science, ICT & Future Planning (MSIP) (NO. NRF-2015R1A5A1037627), and by the KIST-UNIST partnership program (1.160097.01/2.160482.01), and by the Global Frontier R&D Program on Center for Multiscale Energy System funded by the National Research Foundation under the Ministry of Science, ICT & Future Planning, Korea (NO. 2012M3A6A7054855).

References

- [1] J.-Y. Kim, K.-W. Lee, J.-S. Lee, D. Kwon, *Surf. Coat. Technol.* 201 (7) (2006) 4278–4283.
- [2] D. Tabor, *The Hardness of Metals*, Oxford University Press, New York, 1951.
- [3] S. Pathak, S.R. Kalidindi, *Mater. Sci. Eng. R. Rep.* 91 (2015) 1–36.
- [4] J.G. Swadener, E.P. George, G.M. Pharr, *J. Mech. Phys. Solids* 50 (4) (2002) 681–694.
- [5] W.D. Nix, H.J. Gao, *J. Mech. Phys. Solids* 46 (3) (1998) 411–425.
- [6] I.J. Spary, A.J. Bushby, N.M. Jennett, *Philos. Mag.* 86 (33–35) (2006) 5581–5593.
- [7] D. Kramer, R.N. Viswanath, J. Weissmuller, *Nano Lett.* 4 (5) (2004) 793–796.
- [8] Y. Ding, Y.J. Kim, J. Erlebach, *Adv. Mater.* 16 (21) (2004) 1897–+.
- [9] K. Hu, D. Lan, X. Li, S. Zhang, *Anal. Chem.* 80 (23) (2008) 9124–9130.
- [10] M.M. Biener, J. Biener, A. Wichmann, A. Wittstock, T.F. Baumann, M. Baeumer, A.V. Hamza, *Nano Lett.* 11 (8) (2011) 3085–3090.
- [11] E. Detsi, Z.G. Chen, W.P. Vellinga, P.R. Onck, J.T.M.D. Hosson, *J. Nanosci. Nanotechnol.* 12 (6) (2012) 4951–4955.
- [12] T. Fujita, P. Guan, K. McKenna, X. Lang, A. Hirata, L. Zhang, T. Tokunaga, S. Arai, Y. Yamamoto, N. Tanaka, Y. Ishikawa, N. Asao, Y. Yamamoto, J. Erlebach, M. Chen, *Nat. Mater.* 11 (9) (2012) 775–780.
- [13] E. Detsi, P. Onck, J.T.M. De Hosson, *ACS Nano* 7 (5) (2013) 4299–4306.
- [14] E. Detsi, E. De Jong, A. Zinchenko, Z. Vukovic, I. Vukovic, S. Punzhin, K. Loos, G. ten Brinke, H.A. De Raedt, P.R. Onck, J.T.M. De Hosson, *Acta Mater.* 59 (20) (2011) 7488–7497.
- [15] S. Punzhin, E. Detsi, A. Kuzmin, J.T.M. De Hosson, *J. Mater. Sci.* 49 (16) (2014) 5598–5605.
- [16] E. Detsi, M. van de Schootbrugge, S. Punzhin, P.R. Onck, J.T.M. De Hosson, *Scr. Mater.* 64 (4) (2011) 319–322.
- [17] K.R. Mangipudi, E. Epler, C.A. Volkert, *Acta Mater.* 119 (2016) 115–122.
- [18] E.-J. Gwak, J.-Y. Kim, *Nano Lett.* 16 (4) (2016) 2497–2502.
- [19] J. Biener, A.M. Hodge, J.R. Hayes, C.A. Volkert, L.A. Zepeda-Ruiz, A.V. Hamza, F.F. Abraham, *Nano Lett.* 6 (10) (2006) 2379–2382.
- [20] A.M. Hodge, J. Biener, J.R. Hayes, P.M. Bythrow, C.A. Volkert, A.V. Hamza, *Acta Mater.* 55 (4) (2007) 1343–1349.
- [21] C.A. Volkert, E.T. Lilleodden, D. Kramer, J. Weissmüller, *Appl. Phys. Lett.* 89 (6) (2006), 061920.
- [22] J. Biener, A.M. Hodge, A.V. Hamza, L.M. Hsiung, J.H. Satcher, *J. Appl. Phys.* 97 (2) (2005), 024301.
- [23] D. Lee, X. Wei, X. Chen, M. Zhao, S.C. Jun, J. Hone, E.G. Herbert, W.C. Oliver, J.W. Kysar, *Scr. Mater.* 56 (5) (2007) 437–440.
- [24] S. Brinckmann, J.-Y. Kim, J.R. Greer, *Phys. Rev. Lett.* 100 (15) (2008).
- [25] J.R. Greer, W.C. Oliver, W.D. Nix, *Acta Mater.* 53 (6) (2005) 1821–1830.
- [26] J. Biener, A.M. Hodge, A.V. Hamza, L.M. Hsiung, J.H. Satcher, *J. Appl. Phys.* 97 (2) (2005).
- [27] Y.-C. Kim, E.-J. Gwak, S.-m. Ahn, J.-i. Jang, H.N. Han, J.-Y. Kim, *Acta Mater.* 138 (2017) 52–60.
- [28] W.C. Oliver, G.M. Pharr, *J. Mater. Res.* 7 (6) (1992) 1564–1583.
- [29] N.J. Briot, T.J. Balk, *Philos. Mag.* 95 (27) (2015) 2955–2973.
- [30] M.C. Shaw, T. Sata, *Int. J. Mech. Sci.* 8 (1966) 469–478.
- [31] L.J. Gibson, M.F. Ashby, *Cellular Solids: Structure and Properties*, 2nd ed. Cambridge University Press, Cambridge, 1997.